Advanced Composites and Hybrid Materials (2019) 2:373–380
https://doi.org/10.1007/s42114-019-00093-9

ORIGINAL RESEARCH

Crystal structure, optical and electronic properties studies on an hybrid multifunctional $MnCl_4$-based material

Said Kassou[1] · Abdesselam Belaaraj[1] · Philippe Guionneau[2] · Riad Shaltaf[3]

Received: 18 September 2018 / Revised: 24 February 2019 / Accepted: 13 March 2019 / Published online: 29 April 2019

Abstract

In this research, the multifunctional organic-inorganic hybrid PEA-$MnCl_4$ [PEA = $(C_6H_5–C_2H_4–NH_3)_2$] was subjected to single-crystal X-ray diffraction, X-ray diffraction powder, UV-visible spectroscopy, scanning electron microscopy (SEM), and density functional theory, using projector augmented wave (PAW), based on U-Hubbard Hamiltonian (DFT+U) investigations. At 293(2) K, PEA-$MnCl_4$ crystallizes in Orthorhombic system, Pbca space group (a = 7.202(5) Å, b = 7.293(5) Å, c = 39.386(5) Å, and Z = 8). The optical study reveals that the compound undergoes an indirect optical transition with phonon-assisted Mn^{2+} d-d transitions in the visible region with an energy gap of about 2.14 eV, due to the internal transition of metal (orbital d). The implementation of the Hubbard U term in the calculation using (GGA+U) approximation allows more comprehension on the material behavior and shows that it keeps the antiferromagnetic state. The energy gap calculated (2.07 eV) is in good agreement with the experimental value. The electronic densities of states were computed and analyzed.

Keywords Metal-halide hybrids · d-d interactions · Optical band gap · Electronic structure · DFT+U calculations

1 Introduction

Metal-halide hybrid organic perovskite (HOP) belong to an interesting class of compounds with general formula $(R-NH_3)_2\ MX_4$, where R is an organic group, X a halogen atom (X = I, Br, Cl) and M a transition metal (Cu, Mn, Co, Zn). They have received increasing attention in the last decade due to their crystal structure diversity and their important optical properties [1–19]. They crystallize from zero- to three-dimensional structures. The bulk materials find considerable application in fabrication of hybrid solar cells in photovoltaic area with 20% efficiency and in thin-film field-effect transistor [20–27]. The 2D organic-inorganic perovskites have attracted increasing attention because of their great environmental stability compared with 3D perovskites. The 2D HOP have drawn attention for their large band gap which can be used as an absorber in solar cells [28–31]. Previous studies show that the 2D hybrid-based solar cells are fit to hold tight 60% of their first power conversion efficiency under lighting after 2250 h and display more moisture tolerance in comparison to their 3D-based solar cells [32]. In addition, the HOP based on manganese atoms find a certain interest for their optical, magnetic, and solid-solid phase transition properties [33, 34]. The correlation between the electronic structures such as gap energy, density of states, and macroscopic properties can benefit from predictive modeling of these materials using density functional theory (DFT+U), since the DFT is a known weakness methodology of d localized electrons. Recently, the DFT+U method was introduced in computational calculation which consists of the correlation between electronic and Hubbard-type model for a subset of states in the system [35]. This implementation enhances the calculation of energetic, electronic, and magnetic properties of metals and semiconducting and insulating materials with d delocalized electron [36–40].

In this work, we report the synthesis, crystal structure, optical properties from the UV-vis spectroscopy, and electronic properties using DFT+U calculations in order to perform structure-properties correlation of the hybrid PEA-$MnCl_4$.

✉ Abdesselam Belaaraj
a.belaaraj@fs-umi.ac.ma

[1] Laboratoire de Physique des matériaux et modélisation des Systèmes, CNRST-URAC 08, Faculté des Sciences, Université Moulay Ismail, 50000 Meknès, Morocco

[2] CNRS, Université de Bordeaux, ICMCB, UPR 9048, F-33600 Pessac, France

[3] Department of Physics, The University of Jordan, Amman 11942, Jordan

Table 1 Crystallographic and structure refinement data for PEA-$MnCl_4$

Empirical formula	C8 H12 Cl2 Mn0.50 N
Formula weight	220.56
Temperature	293(2) K
Wavelength	0.71073 Å
Crystal system	Orthorhombic
Space group	Pbca
Unit cell parameters	$a = 7.202(5)$ Å
	$b = 7.293(5)$ Å
	$c = 39.368(5)$ Å
Volume	2068(2) $Å^3$
Z	8
Density (calculated)	1.417 g/cm^3
Absorption coefficient	1.155 mm^{-1}
$F(000)$	908
Crystal size	$0.3 \times 0.5 \times 0.03$ mm^3
θ range data collection	3.51°–27.50°
Index ranges	$-9 \le h \le 9$
	$-9 \le k \le 9$
	$-50 \le l \le 50$
Reflections collected	2330
Independent reflections	1759
Completeness to (θ)	26.36°–99.5°
Absorption correction	Empirical
Refinement method F2	Full matrix
Data/restraints/parameters	2330/107/0
Goodness-of-fit on F2	1.168
Final R indices [$I > 2\ \sigma(I)$]	R1 = 0.0645, wR2 = 0.0924
R indices (all data)	R1 = 0.0436, wR2 = 0.0863

2 Experimental

2.1 Synthesis of PEA-$MnCl_4$

Under ambient conditions, PEA-$MnCl_4$ single crystals have been successfully synthesized by the reaction between $MnCl_2$ and $((C_6H_5C_2H_4NH_2)HCl)$ giving $(C_6\ H_5C_2H_4NH_3)_2MnCl_4$. Firstly, phenylethylamonium $(C_6H_5C_2H_4NH_2)$ was protonated by HCl (37%) in 5 ml of water/ethanol (1:1 in the ratio) solution. The solvent was evaporated until a white crystal powder is precipitated as $(C_6H_5C_2H_4NH_2)HCl$. Then a saturated solution of the ammonium salts and $MnCl_2$ powder was prepared. The mixture between these solutions was carried out at room temperature in a glass tube. Pink plate-shaped crystals are obtained after a few weeks.

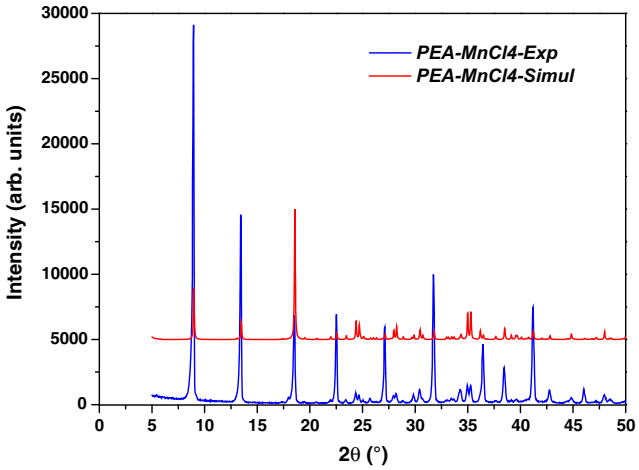

Fig. 1 Experimental and simulated X-ray diffraction patterns of PEA-$MnCl_4$

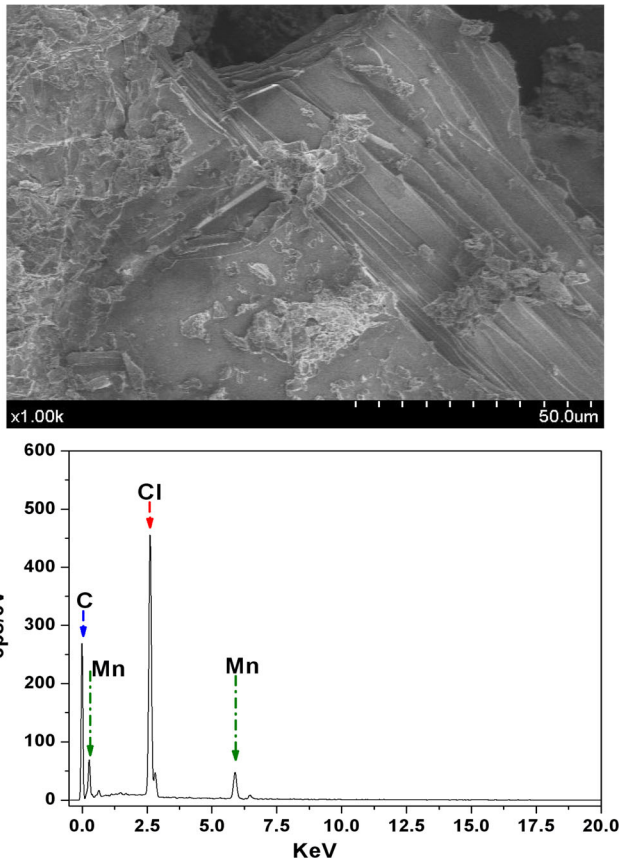

Fig. 2 SEM image (top) and EDX spectrum (bottom) of PEA-$MnCl_4$

2.2 Characterization of PEA-$MnCl_4$

2.2.1 Single-crystal X-ray diffraction data collection

A PEA-$MnCl_4$ single crystal of size $0.3 \times 0.5 \times 0.03$ mm^3 was selected under a polarizing microscope. The measurements were carried out, at 293 K, on a Nonius Kappa CCD diffractometer using Mo-Kα radiation ($\lambda = 0.71073$ Å) from graphite monochromator. The collection data was made using a mixture of Φ and Ω scan modes. The crystal to detector distance was 35.30 mm. The structure was solved by the direct method using SIR97 [41] program refined by the fully matrix least squares technique F^2 using SHELX97 [42]. The non-hydrogen atoms were refined anisotropically and the hydrogen atoms were placed theoretically. All above programs were used within the WINGX package [43] and the drawings were made with Diamond [44]. The crystallographic data and experimental parameters for the intensity collection are summarized in Table 1.

Table 2 Atomic positions displacement (A) of Mn, Cl, N, C atoms for PEA-$MnCl_4$

	Δxx	Δyy	Δzz
Mn	0.00000	0.00000	0.00000
Cl1	0.02051	0.03483	0.00038
Cl2	0.00311	0.00256	0.00574
N	0.00570	0.01545	0.00051
C	0.04877	0.05767	0.00604
C	0.00761	0.00481	0.00493
C	0.01490	0.00258	0.00032
C	0.02405	0.06564	0.00170
C	0.01145	0.01458	0.00792
C	0.00482	0.00991	0.00345
C	0.01892	0.01239	0.00378
C	0.01771	0.01643	0.00046

2.2.2 X-ray powder diffraction

The powder X-ray diffraction pattern of the compound was performed on a LabX XRD-6100 Shimadzu powder X-ray diffractometer using graphite monochromator Cu–Kα radiation. The scanning step was 0.05 in the 2θ angle ranging from 5° to 50°. The experimental and simulated X-ray diffraction patterns represented in Fig. 1 are in good, which confirms the crystalline purity of the prepared compound.

2.2.3 Morphology SEM-EDX

The morphology of the sample was observed by a JSM-6400 electron microscope (JEOL, Japan) with an acceleration voltage of 40 kV. The SEM image (Fig. 2) analysis shows good sample reactivity and good dispersion of the elements at the

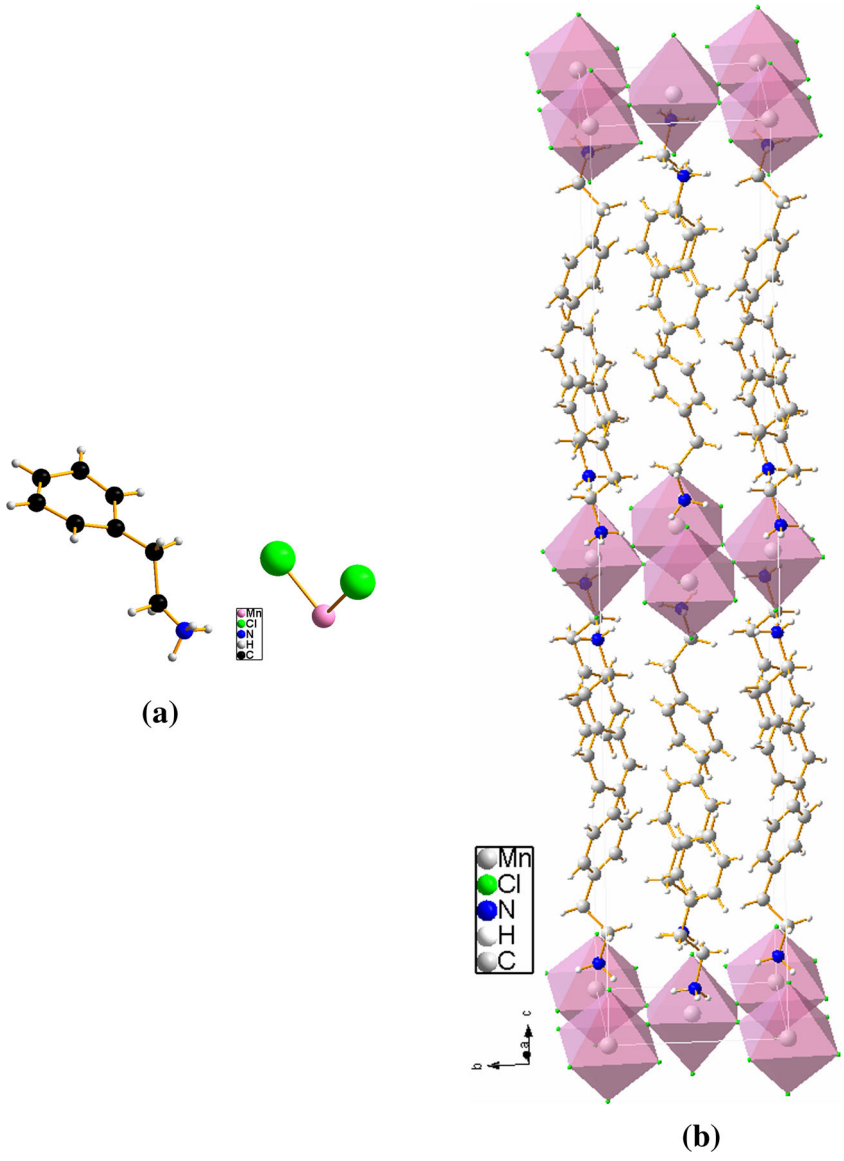

Fig. 3 Overall crystal structure: **a** asymmetric unit cell and **b** projection along *a*-axis (2D structure)

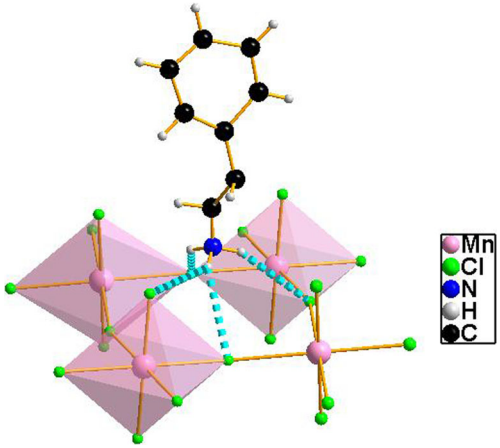

Fig. 4 Hydrogen interaction

micrometric scale, as well as the surface of the hybrid appears in the form of the sheets for this compound and the crystallization is carried out without secondary phase training. The EDX microanalysis associated with the SEM, carried out on the zones of high contrast, shows the presence of characteristic carbon signal (Kα = 0.277 keV) and chlorine (Kα = 2.621 keV), characteristic signal of Mn (Kα = 5.894 keV and Lα = 0.637 keV). Note also the absence of impurities in the studied phase and the conformity and homogeneity of the analyzed composition with that desired.

2.2.4 UV-vis analysis

The UV-vis diffuse reflectance spectrum of PEA-$MnCl_4$ crystal was carried out on a Jasco v-570 spectrophotometer in the range 200–1200 nm. A barium sulfate ($BaSO_4$) plate was used as the standard (100% reflectance) on which the finely ground sample from the crystal was coated. The optical density was calculated from the reflectance spectrum, while the absorption spectrum was calculated using the Kubelka–Munk function [45].

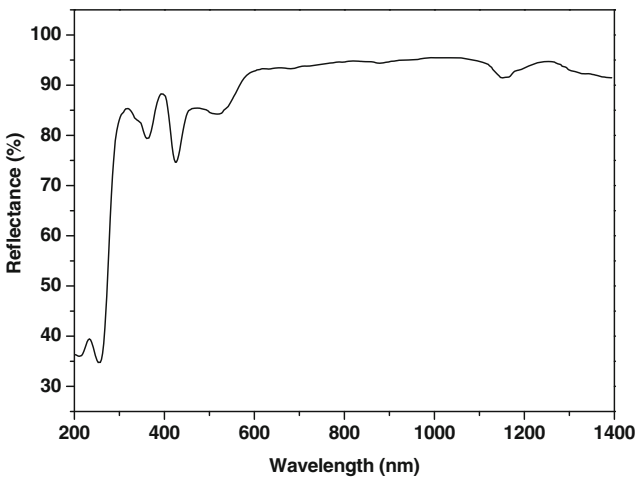

Fig. 5 Reflectance spectrum of PEA-$MnCl_4$

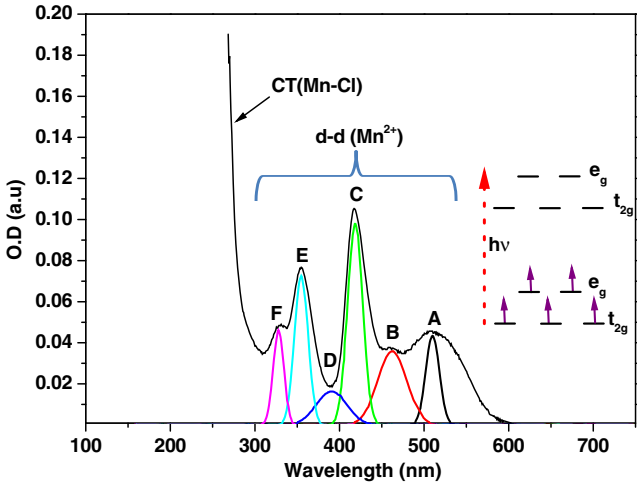

Fig. 6 Optical density of PEA-$MnCl_4$ (CT, charge transfer; d-d: internal transitions between d orbitals)

3 Computational details

All the calculations have been performed using the projector augmented wave (PAW) method with the generalized (GGA-PBE) [46] gradient approximation using U-Hubbard (GGA+U) implemented in the ABINIT code [47]. The Brillouin-zone integration (4 × 4 × 1) was performed using special k points sampled within the Monkhorst–Pack scheme [48]. Khon–Sham orbitals were expanded using a plane wave basis up to a kinetic energy cutoff equal to 23 Ha. Those experimental lattice parameters and atomic positions were used as a starting point for the optimization of atomic positions. The atomic positions within the unit cell relaxed until the forces were less than 0.01 eV/A. The displacement parameters Δ (Δxx, Δyy, Δzz) along the tree axis between experimental and optimized atomic positions are shown in Table 2.

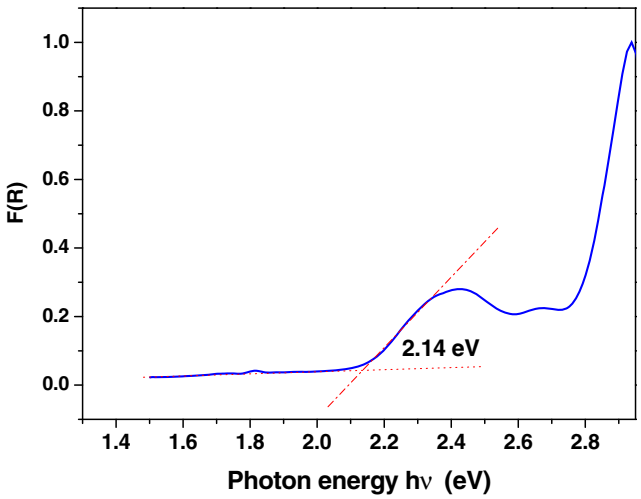

Fig. 7 Kubelka–Munk function versus photon energy for PEA-$MnCl_4$

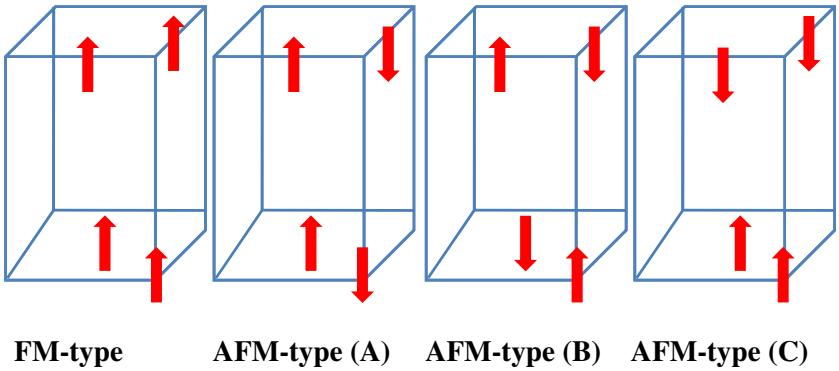

Fig. 8 Different magnetic configurations

4 Results and discussion

4.1 Crystal structure description

The crystal structure has been redetermined in order to gain more accurate values, for bonds and angles within $[MnCl_4]^{2-}$ anion and intermolecular interactions. The compound crystallizes in the orthorhombic system Pbca (n°61) space group with the cell parameters $a = 7.202(5)$ Å, $b = 7.293(5)$ Å, $c = 39.368(5)$ Å, and $Z = 8$ at 293(2) K. These parameters are in good agreement with those of previous study [34]. The asymmetric unit contains one half of $[MnCl_4]^{2-}$ anion and one $(C_6H_5C_2H_4NH_3)^{2+}$ cation as shown in Fig. 3a.

The overall structure consists of alternating organic and inorganic layers, where the inorganic layer form 2D network, interplayed by the $(C_6H_5C_2H_4NH_3)$ bilayer ions (Fig. 3b). The octahedral manganese (II) center is coordinated by six terminal Cl^- ions. The Mn-Cl distances are 2.5754(14) Å and 2.4816(7) Å for equatorial ligands and 2.5744 Å for the axial ones. The bridges angle (Mn-Cl-Mn) is 168.701(28)° which is not linear. The obtained values are in the same order to those of the previous study [34], which are respectively 2.577 Å and 2.484 Å for bond length and 168.66° for angle bridges. The Baur distortion [49] indices (ID) were calculated for PEA-$MnCl_4$, using the formalism of Baur. The obtained indices are $ID(d) = 1.66 \times 10^{-2}$ for distances and $ID(\varphi) = 6.2 \times 10^{-3}$ for angles. These values are lower than those obtained for the compound $(C_6H_9N_2)_2HgCl_4$ [50] ($ID(d) = 1.75 \times 10^{-2}$; $ID((\varphi)) = 3.95 \times 10^{-2}$) indicating a significant higher symmetry in the $[MnCl_4]^{2-}$ entity. Figure 4 displays the hydrogen bond connectivity N-H…Cl between the $[MnCl_6]$ octahedra and the $(C_6H_5C_2H_4NH_3)^+$ cation. H bond is mainly involved in the cohesion of the crystal (Fig. 4). The N…Cl distances are in the range 3.295(3) Å to 3.488(3) Å. Another kind of interactions exists between the inorganic layers assured by van der Waals interactions. In the phenylethylamonium cation, the C-C distances are in the range 1.333(6) Å to 1.379(5) Å for benzene rings and in average of 1.498(4)°A for the alkyl ammonium when the C-C-C average angle is about 118.9(3)° and the torsion angle C-C-C-N is about 172.3(2)°.

4.2 Optical properties

Figure 5 shows the optical reflectance spectrum of PEA-$MnCl_4$ recorded in the range 200 to 1400 nm at room temperature. As it can be seen from the figure, a high reflectance is observed in the range 280–1400 nm (up than 70%) with the appearing of some anomalies in the range of 300–580 nm due to absorption phenomena.

The study of optical properties, such as optical transitions and electronic band structure, near the absorption edge in the UV-Vis region is of major importance. The optical density spectrum of PEA-$MnCl_4$ in the visible and near infrared range, measured at room temperature, is shown in Fig. 6, which shows also decomposition in Gaussian peaks labeled A, B, C, D, E, and F centered at 530, 460, 431, 381, 356, and 326 nm, respectively. These bands can be assigned to the transitions of Mn^{2+} ions in octahedral symmetry [51].

Using Tanabe–Sugano diagram [52] for d^5 configuration and from the literature [53–55], we can attributed the bands A and B to the transition from ground state $^6A_{1g}(S)$ to $^4T_{1g}(G)$ and to $^4T_{2g}(G)$, respectively, where the C and D are assigned to the transition from $^6A_{1g}(S)$ to the excited $^4A_{1g}(G)$ and $^4E_g(G)$ states and from $^6A_{1g}(S)$ to the excited $^4T_{2g}(D)$ states, respectively. The bands E and F are attributed to the transitions from ground state to the excited $^4E_g(D)$ and $^4T_{1g}(P)$ states, respectively.

The optical band gap was determined to inquire the conductivity of PEA-$MnCl_4$ as the intersection point between the energy axis and the line extrapolated from the linear portion of the absorption edge in a plot of Kubelka–Munk function F(R) shown in Fig. 7. According to the previous equation, we found

Table 3 Total energies of different magnetic configurations

	FM	AFM type (A)	AFM type (B)	AFM type (C)
Total energy (eV)	− 25,012.821	− 28,824.694	− 29,751.737	− 30,061.539

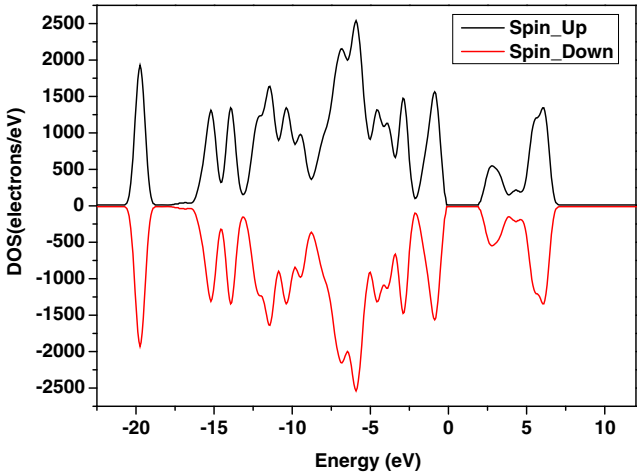

Fig. 9 Total density states

an optical energy gap of about 2.14 eV characteristic of semiconductor materials with a wide band gap.

4.3 Electronic properties

The total energies of different magnetic state configurations (Fig. 8) are gathered in the Table 3.

By comparing the total energy in different magnetic configurations (FM, ferromagnetic; AFM, antiferromagnetic), it is found that the studied hybrid keeps the antiferromagnetic state according to the experimental results [34], although the antiferromagnetic configuration type (C) presents the stable ground state than the configurations AFM type (A) and AFM type (B).

The total density of states (TDOS) for the spin up and spin down of PEA-$MnCl_4$ in antiferromagnetic states type (C) with Hubbard parameter (U_{eff} = 4 eV) is shown in Fig. 9. The analysis along energy axis reveals that the studied hybrid exhibits a semiconductor behavior with a band gap energy of about 2.07 eV, which is slightly smaller than the experimental value (2.14 eV). This underestimation of the band gap energy is explained by an usual artifact of DFT computations. Both experimental and computed values are in the same order than the similar compound $NH_3(CH_2)_5NH_3MnCl_4$ [56].

To gain more insight into the bonding between all atoms, we have calculated the partial density of states (PDOS) of each atom (Fig. 10). The analysis of the density contribution in the valence band (VB) and the conduction band (CB) reveals that the maximum valence band (MVB) consists mainly of the orbital contribution Mn-d for spin up and spin down. Low

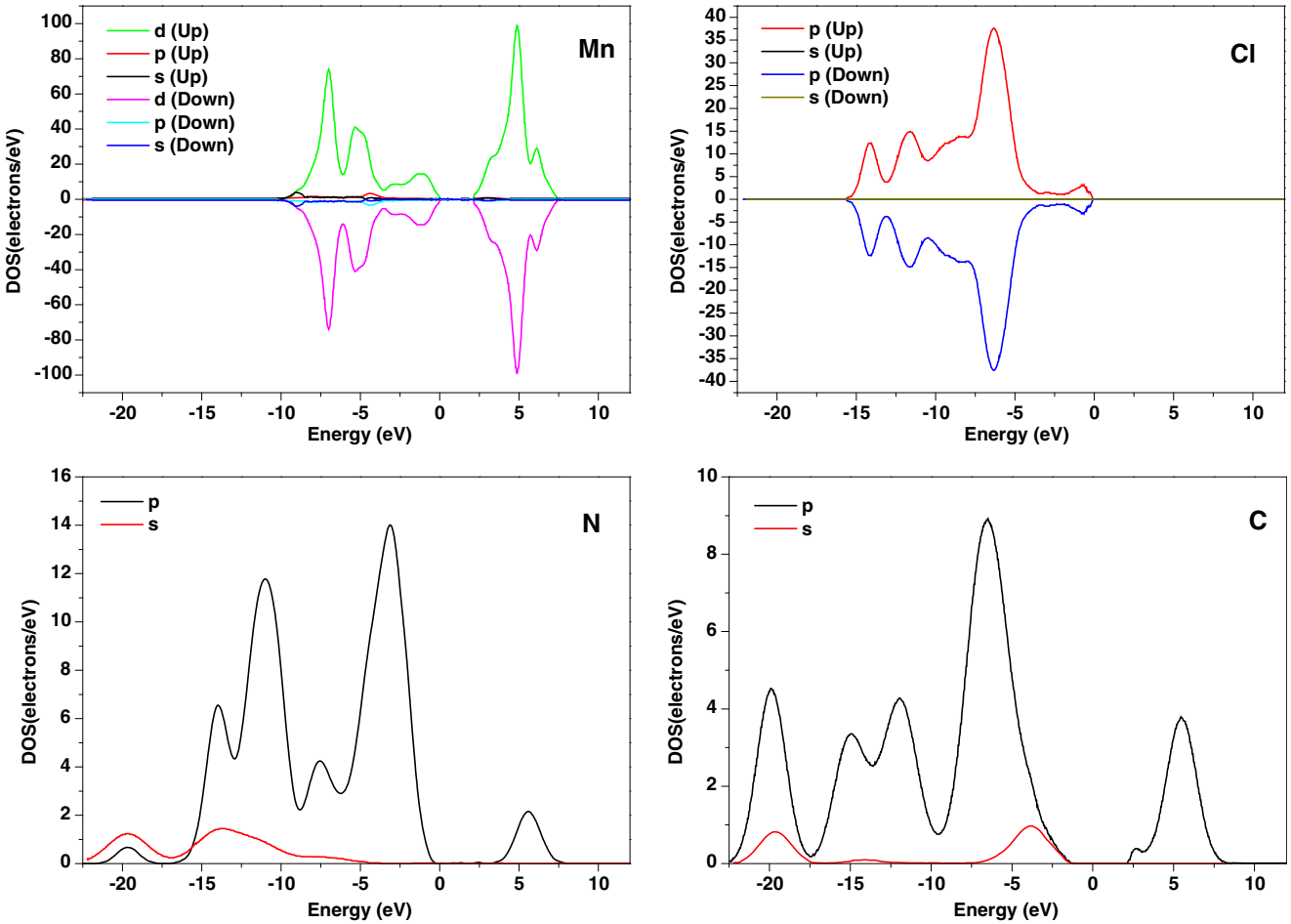

Fig. 10 Calculated PDOS diagram

contributions of Mn-s, Mn-p, N-p, and Cl-p orbitals are shown too. While the minimum of the conduction band (MCB) consists of the d-orbital up-down spin of Mn, N-2p, and C-2p orbitals. We can also show that the orbitals C-2s, C-2p, N-2s, and N-2p contribute around − 20 eV. However, the contribution of the various components (Mn-s, Mn-p, Mn-d, Cl-s, Cl-p, N-s, N-p, C-s, and C-p) is observed in the energy range [− 15, 0] eV.

5 Conclusion

In this work, we have synthesized the organic-inorganic hybrid $[C_6H_5C_2H_4NH_3]_2MnCl_4$ single crystals by slow evaporation at room temperature. The crystal structure, morphology and the purity of the compound were checked using single-crystal X-ray diffraction, SEM-EDX, and powder XRD analysis. The crystal structure consists of infinite chains forming a 2D framework. The optical density spectrum recorded in UV-vis shows six peaks assigned to the Mn^{2+} ions d-d transitions in the octahedral symmetry. The electronic properties were investigated by the high-throughput performed DFT+U calculation using PAW method, The different magnetic configurations calculated reveal the antiferromagnetic behavior of the studied material. The hybrid has an indirect band gap materiel, with a band gap energy of about 2.07 eV, which is slightly lower than the experimental value (2.14 eV). The analysis of the partial densities of states (PDOS) of each atom reveals the contribution of different atomic orbitals, to the maximum of the valence band (MVB) and the minimum of the conduction band (MCB).

Acknowledgements This work was initiated with the support of URAC08, Project RS:02 (CNRST, Morocco). We also thank Prof. S. Aït Lyazidi and Prof. M. Haddad, LASMAR Laboratory, Moulay Ismail Univ. Morocco, for recording optical measurements.

Compliance with ethical standards

Conflict of interest The authors declare that they have no conflict of interest.

References

1. Mitzi DB (2007) Syntesis and propreties of organic-inorganic perovskites and related materials. Prog Inorg Chem 48:1
2. Zhang S, Lanty G, Lauret JS, Deleporte E, Audebert P, Galmichem L (2009) Synthesis and optical properties of novel organic-inorganic hybrid nanolayer structure semiconductors. Acta Mater 57:3301
3. Ionescu D, Ciobanu I, Radinschi I (2007) Frequency resonant behaviour of the effective permittivity for a polyvalent liquid crystal in microwave range. J Optoelectron Adv M 9:2608
4. Zhang S, Audebert P, Wei Y, Lauret JS, Galmiche L, Deleporte E (2010) Synthesis and optical properties of novel organic-inorganic hybrid UV $(R\text{-}NH_3)_2PbCl_4$ semiconductors. J Mater Chem 21:466
5. El Mrabet R, Kassou S, Tahiri O, Balaaraj A, Guinneau P (2016) Theoretical and experimental investigations of optical, structural and electronic properties of the lower dimensional hibrid $[NH_3\text{-}(CH_2)_{10}\text{-}NH_3]$ $ZnCl_4$. Eur Phys J Plus 131:369
6. Gu H, Liu C, Zhu J, Gu J, Wujcik EK, Shao L, Wang N, Wei H, Scaffaro R, Zhang J, Guo Z (2018) Introducing advanced composites and hybrid materials. Adv Comp Hybrid Mater 1(1):1
7. Mostafa M, El-Khiyami S (2014) Crystal structure and electric properties of the organic–inorganic hybrid: $[(CH_2)_6(NH_3)_2]ZnCl_4$. J Solid State Chem 209:82
8. Kulicka B, Jakubas R, Ciunik Z, Bator G, Medycki W, wiergiel J, Baran J (2004) Structure, phase transitions and molecular dynamics in 4-methylpyridinium tetrachloroantimonate(III), [4-CH3C5H4NH][SbCl4]. J Phys Chem Solids 65:871
9. Kassou S, Kaiba A, Guinneau P, Balaaraj A (2016) Organic-inorganic hybrid perovskite $(C_6H_5(CH_2)_2NH_3)_2CdC_{l4}$: synthesis, structural and thermal properties. J Struct Chem 57:737
10. Mohamed CB, Karoui K, Saidi S, Guidara K, Rhaiem AB (2014) Electrical properties, phase transitions and conduction mechanisms of the $((C_2H_5)NH_3)_2CdCl_4$ compound. Physica B 451:87
11. Kalyanaraman S, Shajinshinu P, Vijayalakshmi S (2015) Refractive index, band gap energy, dielectric constant and polarizability calculations of ferroelectric Ethylenediaminium Tetrachlorozincate crystal. J Phys Chem Solids 86:108
12. Baikie T, Fang Y, Kadro JM, Schreyer M, Wei F, Mhaisalkar SG, Gräetzel M, White TJ (2013) Synthesis and crystal chemistry of the hybrid perovskite $(CH_3NH_3)PbI_3$ for solid-state sensitised solar cell applications. J Mater Chem A1:5628
13. Benedek NA, Rondinelli JM, Djani H, Ghosez P (2015) Understanding ferroelectricity in layered perovskites: New ideas and insights from theory and experiments. Dalton Trans 44:10543
14. Kassou S, El Mrabet R, Kaiba A, Guinneau P, Balaaraj A (2016) Combined experimental and density functional theory studies of an organic-inorganic hybrid perovskite. Phys Chem Chem Phys 18: 9431
15. Cheng Z, Lin J (2010) Layered organic–inorganic hybrid perovskites: structure, optical properties, film preparation, patterning and templating engineering. CrystEngComm. 12:2646
16. Wei Y, Audebert P, Galmiche L, Lauret JS, Deleporte E (2013) Synthesis, optical properties and photostability of novel fluorinated organic–inorganic hybrid $(R\text{–}NH_3)_2PbX_4$ semiconductors. J Phys D Appl Phys 46:135105
17. González-Carrero S, Galian RE, Pérez-Prieto J (2015) Organometal Halide Perovskites: Bulk Low-Dimension Materials and Nanoparticles. Part Part Syst Charact 32:709
18. Gómez-Romero P, Sanchez C (2005) Functional hybrid materials. Wiley-VCH Verlag GmbH & Co. KGaA, Weinheim
19. Kayan A (2018) Inorganic-organic hybrid materials and their adsorbent properties. Adv Comp Hybrid Mater 1(1):1
20. Wu Y, Li J, Xu J, Du Y, Huang L, Ni J, Cai H, Zhang J (2016) Organic–inorganic hybrid $CH_3NH_3PbI_3$ perovskite materials as channels in thin-film field-effect transistors. RSC Adv 20:16243
21. Even J, Pedesseau L, Katan C (2014) Analysis of multivalley and multibandgap absorption and enhancement of free carriers related to exciton screening in hybrid perovskites. J Phys Chem C 118: 11566
22. Kundys B, Lappas A, Viret M, Kapustianyk V, Rudyk V, Semak S, Simon C, Bakaimi I (2010) Multiferroicity and hydrogen-bond ordering in $(C_2H_5NH_3)_2CuCl_4$ featuring dominant ferromagnetic interactions. Phys Rev B 81:224434
23. Chen Q, De Marco N, Yang YM, Song TB, Chen CC, Zhao H, Hong Z, Zhou H, Yang Y (2015) The organic-inorganic hybrid

halide perovskite for optoelectronic applications. Nano Today 10: 355
24. Matsuishi K, Ishihara T, Onari S, Chang YH, Park CH (2004) Optical properties and structural phase transitions of lead-halide based inorganic-organic 3D and 2D perovskite semiconductors under high pressure. Phys Status Solidi B 241:3328
25. Bassani F, La Rocca GC, Agranovich VM (2000) Organic-inorganic junctions and microcavities: new effects and applications. Int J Quantum Chem 77:973
26. Veldhuis SA, Boix PP, Yantara N, Li M, Sum TC, Mathews N, Mhaisalkar SG (2016) Perovskite materials for light-emitting diodes and lasers. Adv Mater 28:6804
27. Sepalage GA, Meyer S, Pascoe A, Scully AD, Huang F, Bach U, Cheng Y-B, Spiccia L (2015) A facile deposition method for CuSCN: exploring the influence of CuSCN on J-V hysteresis in planar perovskite solar cells. Adv Funct Mater 25:5650
28. Smith IC, Hoke ET, Solis-Ibarra D, McGehee MD, Karunadasa HI (2014) A layered hybrid perovskite solar-cell absorber with enhanced moisture stability. Angew Chem Int Ed 53:11232
29. Bischak CG, Sanehira EM, Precht JT, Luther JM, Ginsberg NS (2015) Heterogeneous Charge Carrier Dynamics in Organic-Inorganic Hybrid Materials: Nanoscale Lateral and Depth-Dependent Variation of Recombination Rates in Methylammonium Lead Halide Perovskite Thin Films. Nano Lett 15:4799
30. Leijtens T, Eperon GE, Noel NK, Habisreutinger SN, Petrozza A, Snaith HJ (2015) Stability of metal halide perovskite solar cells. Adv Energy Mater 5:1500963
31. Kazim S, Nazeeruddin MK, Grätzel M, Ahmad S (2014) Perovskite as light harvester: a game changer in photovoltaics. Angew Chem Int Ed 53:2812
32. Chen Y, Sun Y, Peng J, Tang J, Zheng K, Liang Z (2018) 2D Ruddlesden-Popper Perovskites for Optoelectronics. Adv Mater 30:1703487
33. Huang B, Zhang JY, Huang RK, Chen MK, Xue W, Zhang WX, Zeng MH, Chen XM (2018) Spin-reorientation-induced magnetodielectric coupling effects in two layered perovskite magnets. Chem Sci 9(37):7413
34. Park S-H, Oh I-H, Park S, Park Y, Kim JH, Huh Y-D (2012) Canted antiferromagnetism and spin reorientation transition in layered inorganic–organic perovskite $(C_6H_5CH_2CH_2NH_3)_2MnCl_4$. Dalton Trans 41:1237
35. Liechtenstein AI, Anisimov VI, Zaanen J (1995) Density-functional theory and strong interactions: Orbital ordering in Mott-Hubbard insulators. Phys Rev B52:R5467
36. Araujo-Lopez E, Varilla LA, Seriani N, Montoya JA (2016) TiO_2 anatase's bulk and (001) surface, structural and electronic properties: A DFT study on the importance of Hubbard and van der Waals contributions. Surf Sci 653:187
37. Curnan MT, Kitchin JR (2015) Investigating the energetic ordering of stable and metastable TiO_2 polymorphs using DFT+U and hybrid functionals. J Phys Chem C119:21060
38. Hu Z, Metiu H (2011) Choice of U for DFT+U calculations for titanium oxides. J Phys Chem C115:5841
39. Cinquini F, Giordano L, Pacchioni G (2006) Electronic structure of ultrathin NiO films on Ag(100) thin films from DFT and hybrid functional DFT approaches. Phys Rev B74:165403
40. Grau-Crespo R, Corá F, Sokol AA, de Leeuw NH, Catlow CRA (2006) Electronic structure and magnetic coupling in FeSbO4: A DFT study using hybrid functionals and GGA+U methods. Phys Rev B73:035116
41. Altomare A, Burla MC, Camalli M, Cascarano GL, Giacovazzo C, Guagliardi A, Moliterni AGG, Polidori G, Spagna R (1999) A new tool for crystal structure determination and refinement. J Appl Crystallogr 32:115
42. Sheldrick M (2007) A short history of SHELX. Acta Cryst A64:112
43. Farrugia L (1999) WinGX-32: systeme of programs for solving, refining and analyzing single crystal X-ray diffraction data for small molecules. J Appl Crystallogr A32:837
44. Brandenburg K (2010) DIAMOND release 3.2c. Crystal Impact GbR, Bonn
45. Džimbeg-Malčić V, Barbarić-Mikočević Ž, Itrić K (2011) Kubelka-Munk theory description in optical properties of paper (I). Technical Gazette 18(1):117
46. Perdew JP, Burke K, Ernzerhof M (1996) Generalized gradient approximation made simple. Phys Rev Lett 77:3865
47. Gonze X, Amadon B, Anglade PM, Beuken JM, Bottin F, Boulanger P, Bruneval F, Caliste D, Caracas R, Cote M, Deutsch T, Genovese L, Ghosez P, Giantomassi M, Goedecker S, Hamann DR, Hermet P, Jollet F, Jomard G, Leroux S, Mancini M, Mazevet S, Oliveira MJT, Onida G, Pouillon Y, Rangel T, Rignanese G-M, Sangalli D, Shaltaf R, Torrent M, Verstraete MJ, Zerah G, Zwanziger JW (2009) ABINIT: first-principales approach to material and nanosystem properties. Comut Phys Commun 180:2582
48. Monkhorst HJ, Pack JD (1976) Special points for Brillouin zone integrations. Phys Rev B13:5188
49. Baur W (1974) The geometry of polyhedral distortions. Predective relationships for phosphate group. Acta Crystallogr Sect B-Struct Sci 30:1195
50. Elwej R, Hannachi N, Chaabane I, Oueslati A, Hlel F (2013) Structural, characterization and AC conductivity of bis-2amino-6-picolinium tetrachloromercurate $(C_6H_9N_2)_2HgCl_4$. Inorg Chim Acta 406:10
51. Raju CL, Gopal NO, Narasimhulu KV, Rao JL, Reddy BV (2005) EPR, optical and infrared absorption studies of Mn^{2+} ions doped in zinc malate trihydrate single crystal. Spectrochim Acta A 61:2181
52. Xiao Tanabe Y, Sugano S (1954) On the absorption spectra of complex ions. I and II. J Phys Soc Jpn 9:766
53. Mehra A, Venkateswarlu P (1966) Absorption spectrum of Mn^{2+} in KCL. J Chem Phys 45:3381
54. Mehra A (1968) Optical absorption of Mn^{2+} doped alkali halides. Phys Status Solidi B 29:847
55. Rao JL, Purandar K (1981) Electronic absorption spectrum of Mn^{2+} ions doped in diglicine barium chloride monohydrate. Solid State Commun 37:983
56. Lv XH, Liao WQ, Li PF, Wang ZX, Mao CY, Zhang Y (2016) Dielectric and photoluminescence properties of a layered perovskite-type organic-inorganic hybrid phase transition compound $NH_3(CH_2)_5NH_3MnCl_4$. J Mater Chem C 4(9):1881